ACS OMEGA

http://pubs.acs.org/journal/acsodf

Article

Electronic and Optical Properties of van der Waals Heterostructures Based on Two-Dimensional Perovskite $(PEA)_2PbI_4$ and Black Phosphorus

Dong Li, Dan Li,* Anqi Yang, He Zhang, Xinxin Lai, and Chunjun Liang*

Cite This: *ACS Omega* 2021, 6, 20877−20886

Read Online

ACCESS | Metrics & More | Article Recommendations | Supporting Information

ABSTRACT: Combining two-dimensional (2D) perovskites with other 2D materials to form a van der Waals (vdW) heterostructure has emerged as an intriguing way of designing electronic and optoelectronic devices. The structural, electronic, and optical properties of the 2D $(PEA)_2PbI_4$/black phosphorus (BP) [PEA:$(C_4H_9NH_3)^+$] vdW heterostructure have been investigated using first-principles calculations. We found that the $(PEA)_2PbI_4$/BP heterostructure shows a high stability at room temperature. It is demonstrated that the $(PEA)_2PbI_4$/BP heterostructure exhibits a type-I band arrangement with high carrier mobility. Moreover, the band gap and band offset of $(PEA)_2PbI_4$/BP can be effectively modulated by an external electric field, and a transition from semiconductor to metal is observed. The band edges of $(PEA)_2PbI_4$ and BP in the $(PEA)_2PbI_4$/BP heterostructure, which show significant changes with the external electric field, provide further support. Furthermore, the BP layers can enhance the light absorption of the $(PEA)_2PbI_4$/BP heterostructures. Our results indicate that the 2D perovskite and BP vdW heterostructures are competitive candidates for the application of low-dimensional photovoltaic and optoelectronic devices.

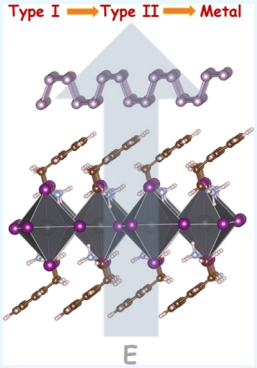

1. INTRODUCTION

In recent years, organic−inorganic hybrid halide perovskites have drawn huge attention because of their fantastic photoelectric properties, for example, low carrier recombination rate, low trap states, high optical absorption coefficient, and high carrier mobility.[1−5] The hybrid perovskites have arisen as the absolute most encouraging materials for optoelectronic applications, including photovoltaics, photodetectors, and light-emitting diodes. Not long ago, single-junction solar cells based on three-dimensional (3D) perovskites have achieved a high power conversion efficiency of 25.2%.[6] Regardless of the fervor, these 3D perovskites suffer from critical stability problems, confining their more extensive business application. On the other side, two-dimensional (2D) Ruddlesden−Popper (RP) hybrid perovskites have been displayed to show superior heat resistance and water resistance relative to the 3D perovskites, which have acquired a lot of attention recently.[7]

2D RP perovskite materials have the general chemical formula A_2BX_4 and comprise stacks of octahedral metal−halide (B−X) monolayers, where B is normally a divalent metal, each isolated by long-chain organic molecules (A) to maintain charge balance.[8−10] In the 2D hybrid perovskites, it requires more energy to destroy the 2D crystal structure due to the large van der Waals (vdW) interaction between organic cations and inorganic anions, which leads to excellent stability contrasting to their 3D counterparts[11,12] Furthermore, 2D perovskites not only enjoy benefits of molecular scale self-assembly, soluble processing, and excellent film formation but also have advantages of excellent optical properties and large carrier diffusion length.[13−15] Tsai et al. fabricated nearly single crystalline 2D perovskite $(BA)_2PbI_4$ with an efficiency of about 12% when used as a solar absorber, indicating that 2D perovskites exhibit superior stability.[16] At the same time, the organic insulating layer also causes the quantum confinement effect, which widens the energy band gap of the 2D material,[17] increases the exciton binding energy, and weakens the optical absorption. These disadvantages lead to the low energy conversion efficiency of 2D perovskite solar cells.[16,18] How to ensure stability and achieve excellent carrier transport performance and high efficiency in 2D perovskite electronic and optoelectronic devices is an urgent problem. Luckily, the exfoliation of multifarious 2D materials in recent years has increased the chance of designing vdW heterostructures, which gives more possibilities for accomplishing wanted electronic or optoelectronic properties.[19,20]

2D materials, for example, graphene and transition metal dichalcogenide (TMD), have incredible potential in next-generation electronic and photonic devices attributable to their outstanding basal physical properties.[21−23] Black phosphorus (BP), a novel 2D isomer of white phosphorus and the most stable one at room temperature, has been successfully prepared

Received: April 30, 2021
Accepted: July 27, 2021
Published: August 5, 2021

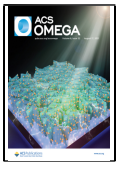

in experiments.[24,25] BP has a finite direct band gap and shows extraordinary electrical and optical properties.[26] The excellent transport properties of BP, such as a high hole mobility up to 1000 $cm^2 V^{-1} s^{-1}$, make BP have potential applications in low dimensional electronics and optoelectronics.[27] Recently, researchers have turned their attention to 2D heterostructures, which are designed by stacking two or more different 2D materials through vdW interactions, such as, G/h-BN,[28] BP/BN,[29] BP/TMDs,[30−32] 2D perovskite/TMDs,[33−36] and MoS_2/SiC.[37] The vdW heterostructures not only break through the application limits of a single material but can also effectively solve the problem of interface disorder in traditional 3D heterojunctions[38−40] In addition, 2D heterostructures have exhibited unique physics as compared with 2D homo-bilayers due to vdW interactions.[41,42] 2D heterostructures can exhibit the characteristics of insulators, semiconductors, metals, semimetals, topological insulators, and superconductors and have broad applications in field-effect transistor fields, photodetectors, electrocatalysis, and energy storage devices.[43−49] For example, Wang et al. demonstrated that tunnel field-effect transistors based on the BP/InSe heterojunction exhibit negative differential resistance and a large on/off current ratio of up to 10^8 when applying low voltages.[50] An anomalous photoluminescence quenching is observed in artificial heterostacking of monolayer TMDs and few-layer BP.[51] Zhang et al. found unexpectedly high photoluminescence enhancement factors of up to ∼8 in vdW heterostructures consisting of the 2D hybrid perovskite $(C_6H_5C_2H_4NH_3)_2PbI_4$ and monolayer WS_2.[36]

However, few theoretical and experimental works report the photoelectric properties of the vdW heterostructure based on 2D perovskites and BP. The physical properties such as the energy band gap and band offsets of the 2D perovskite/BP heterostructure are also totally unknown, while band offsets of semiconducting heterostructures are important and required factors in the design of materials and devices. Herein, in this paper, the 2D RP hybrid perovskite, $(PEA)_2PbI_4$ [PEA: $(C_4H_9NH_3)^+$], was selected to construct a heterostructure with monolayer BP. The geometric, electronic, and optical properties of the $(PEA)_2PbI_4$/BP heterostructure were investigated by density functional theory (DFT) calculations. Our outcomes show that $(PEA)_2PbI_4$ interacts generally feebly with BP using vdW force, and hence, the inborn properties of both 2D $(PEA)_2PbI_4$ perovskites and BP are held in the vdW heterostructure. In this work, we found that the $(PEA)_2PbI_4$/BP heterostructure shows type-I band alignment. Moreover, tunable band gaps and a phase transition from semiconductor to metal can be observed via an external electric field in the $(PEA)_2PbI_4$/BP heterostructure. Besides, the light absorption coefficient of the $(PEA)_2PbI_4$/BP heterostructures can be effectively improved by monolayer BP. These results indicate that the 2D perovskite and BP vdW heterostructures are competitive candidates for the application of low-dimensional photovoltaic and optoelectronic devices. Our results are of great importance for experimentally understanding and modulating the physical properties of 2D perovskite/BP vdW heterostructures, which can pave the way for the application of 2D perovskite/BP vdW heterostructures.

2. COMPUTATIONAL METHODS

The DFT calculations were performed using the Vienna Ab initio Simulation Package (VASP)[52] with electron−ion interaction described by the projector augmented wave (PAW) methods.[53] The Perdew−Burke−Ernzerhof (PBE) methods under the generalized gradient approximation (GGA) were chosen to describe the exchange and correlation effects of valence electrons.[54] Taking into account the effect of intermolecular forces in the calculation results, the zero damping DFT-D3 method of Grimme was used to deal with vdW force correction in VASP.[55] The valence electron configurations of H ($1s^1$), C ($2s^22p^2$), N ($2s^22p^3$), Pb ($5d^{10}6s^26p^2$), P ($3s^23p^3$), and I ($5s^25p^5$) were adopted in calculations. A cut-off energy of 500 eV, 6 × 12 × 1 *k*-point mesh, and 1×10^{-5} eV total energy convergence tolerances were applied during static calculation. The thickness of the vacuum was set to larger than 15 Å to eliminate the interaction between slabs. Here, none of the spin−orbit coupling and HSE06 functional were considered for the calculation of the electronic structures due to error cancellation; that is, neglecting the spin−orbit interaction caused band gap overestimation, which cancels the underestimation error of GGA calculation.[56−59] Also, the ab initio molecular dynamics (AIMD) simulation was performed by using the PAW method and PBE-GGA implemented in VASP. The *NVT* (constant number of atoms *N*, volume *V*, and temperature *T*) ensemble with the Nose−Hoover thermostat was used during AIMD simulation.[60] An external pressure of 10^5 Pa, a temperature of 300 K, and a time step of 1 fs were set.

To determine the interaction between BP and $(PEA)_2PbI_4$, the binding energy between the BP layer and the $(PEA)_2PbI_4$ layer is calculated as follows

$$E_b = E_{(PEA)_2PbI_4/BP} - E_{BP} - E_{(PEA)_2PbI_4}$$

where $E_{(PEA)_2PbI_4/BP}$ is the total energy of the $(PEA)_2PbI_4$/BP vdW heterostructure and E_{BP} and $E_{(PEA)_2PbI_4}$ are the total energies of the isolated single-layer BP and isolated single-layer $(PEA)_2PbI_4$, respectively.

The carrier mobility was calculated based on the following expression

$$\mu_{2D} = \frac{e\hbar^3 C_{2D}}{k_B T m^* m_a^* E_i^2}$$

where m^* is the effective mass on the calculating direction *x* or *y*, which is given as

$$m^* = \frac{\hbar^2}{\frac{\partial^2 E_0(k)}{\partial k^2}}$$

where E_0 is the band energy at conduction band minimum (CBM) or valence band maximum (VBM) and m_a^* is the averaged effective mass given by $m_a^* = \sqrt{m_x^* m_y^*}$. E_i is the deformation potential constant given by $E_i = \frac{\Delta V_i}{(\Delta l / l)}$, where ΔV_i represents the energy change of CBM or VBM. C_{2D} is the in-plane elastic modulus (in both *x*- and *y*-directions), which can be derived from

$$\frac{E - E_0}{S_0} = \frac{C_{2D}}{2}\left(\frac{\Delta l}{l_0}\right)^2$$

where $E - E_0$ represents the total energy change, S_0 is the area of the *xy* plane, and Δl represents the deformation in the *x*- or *y*-direction. Figure S2 shows the energy shifts of the band edge position (ΔE_{edge}) at VBM and CBM of the $(PEA)_2PbI_4$/BP

https://doi.org/10.1021/acsomega.1c02264
ACS Omega 2021, 6, 20877−20886

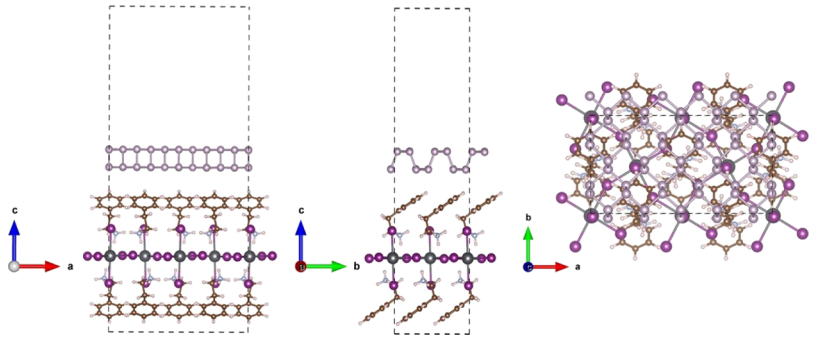

Figure 1. Side and top views of the $(PEA)_2PbI_4$/BP heterostructure. A vacuum larger than 15 Å was set along the *z*-direction. I, Pb, C, N, P, and H atoms are represented by the purple, gray, brown, cyan, silver, and smallest spheres, respectively.

heterostructure with the applied strain along the *a*- and *b*-directions, respectively. The deformation potential constant E_i may be calculated by simulating the linear relationship between band edge energy and strain (δ) exerted in the *a*- and *b*-directions. Figure S3 shows the relationship between the total energy and lattice strain in the *a*- and *b*-directions of the $(PEA)_2PbI_4$/BP heterostructure. The absorption coefficient is calculated from the dielectric function using the following expression

$$\alpha(\omega) = \sqrt{2}\,\omega[\sqrt{\varepsilon_1(\omega)^2 + \varepsilon_2(\omega)^2} - \varepsilon_1(\omega)]^{1/2}$$

where $\varepsilon_1(\omega)$ and $\varepsilon_2(\omega)$ are the real and imaginary parts of the dielectric function, respectively, and are determined by the optical frequency ω.

3. RESULTS AND DISCUSSION

3.1. Geometric Structure. Table S1 shows the calculated lattice parameters of the $(PEA)_2PbI_4$ and BP monolayers, respectively. The optimized lattice constants of monolayer $(PEA)_2PbI_4$ are a = 8.44 and b = 8.76, respectively, and the estimated lattice constants of monolayer BP are a = 3.30 and b = 4.59, both of which are congruent with theoretical and experimental results.[26,31,61,62] Figure 1 shows the intended structure of the $(PEA)_2PbI_4$/BP heterostructure. A supercell in such a system is made up of 5 × 2 BP unit cells and 2 × 1 $(PEA)_2PbI_4$ unit cells. The heterostructure's lattice constants are a = 16.68 Å and b = 8.97 Å, resulting in a < 3% total induced strain in both the BP and $(PEA)_2PbI_4$ lattices.

Geometry optimization was split into two processes for the sake of accuracy and computational efficiency. We start by changing the interlayer distance and calculating the binding energy and then fitting the results into the well-known Buckingham potential equation, as shown below[63,64]

$$E_b = A\,e^{-Bh} - \frac{C}{h^6}$$

A, *B*, and *C* are fitting parameters, *h* is the interlayer spacing, and E_b is the interlayer binding energy. Figure 2 depicts the binding energy as a function of interlayer distance and fitting curve. The fitting curve predicts an equilibrium interlayer distance of around 2.81 Å. Step two involves building a structure with an interlayer distance of 2.81 Å and putting it through a full relaxation to get the final equilibrium structure. The fully optimized structure's averaged interlayer gap between the monolayer BP and $(PEA)_2PbI_4$ is 2.84 Å, which is obviously greater than the bond length of C−H atoms (1.1 Å) or P−P atoms (2.2 Å). The interface contact in the 2D

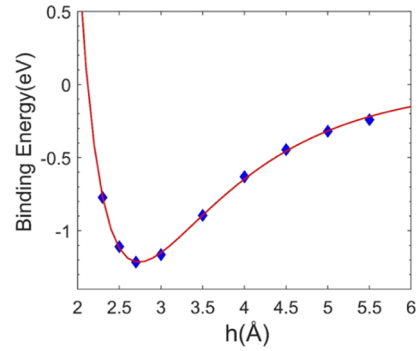

Figure 2. Calculated interlayer binding energies as a function of a series of interlayer spacing and Buckingham potential fitting curve.

$(PEA)_2PbI_4$/BP heterostructure is vdW interaction, with an interlayer binding energy of 1.30 eV, according to the data. The fully optimized structure was used to calculate the energy band, the density of states (DOS), and other results. The *NVT* ensemble lattice dynamics simulations are performed at room temperature to further test the thermodynamic stability of a completely optimized structure. The time-dependent total energies are fluctuating within a restricted energy range generated by temperature after 3 ps, as illustrated in Figure 3, indicating that there is no phase transition for the material at room temperature and the material is thermally stable at room temperature.

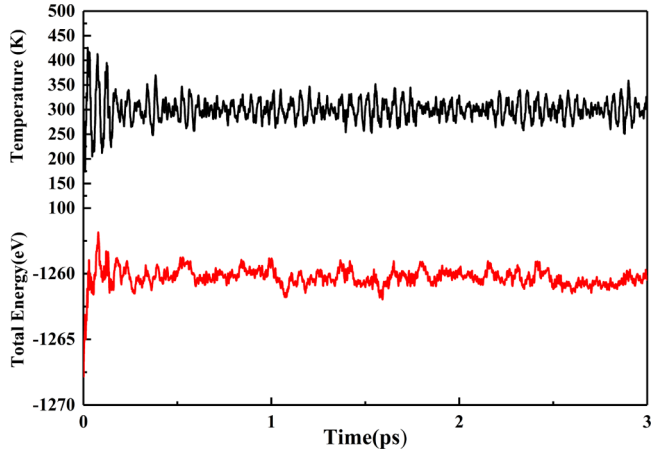

Figure 3. Energy change and the temperature change of the $(PEA)_2PbI_4$/BP heterostructure after AIMD simulation of 3 ps and under 300 K and 10^5 Pa.

https://doi.org/10.1021/acsomega.1c02264
ACS Omega 2021, 6, 20877−20886

3.2. Electronic Properties. We first calculate the band structures of monolayer $(PEA)_2PbI_4$ and monolayer BP to better understand the electronic characteristics of the $(PEA)_2PbI_4$/BP heterostructure. The calculated band structure of the 2D perovskite $(PEA)_2PbI_4$ possesses a direct band gap of 2.17 eV, while the monolayer BP exhibits a direct band gap of 0.86 eV, as shown in Figure S1a,b, respectively. Our obtained above band gap agrees well with previous reports.[31,32,62] Figure 4 depicts the projected band structure

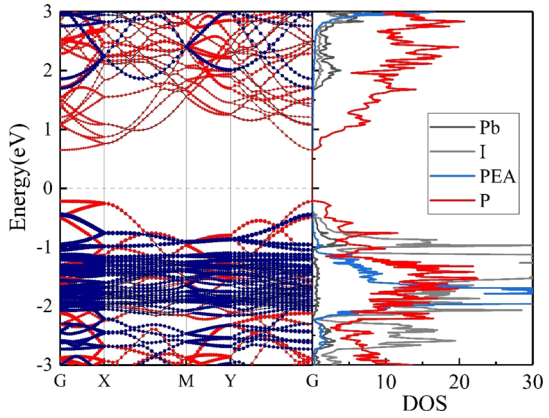

Figure 4. Calculated projected band structure and projected DOS of the $(PEA)_2PbI_4$/BP heterostructure; the bands projected onto $(PEA)_2PbI_4$ and BP are depicted blue and red, respectively. The size of the dots in the bands corresponds to the weight of each species in the bands. The Fermi level (the dotted line) is set to zero.

for the $(PEA)_2PbI_4$/BP vdW heterostructure. It means that in this heterostructure, the electronic structures of monolayer $(PEA)_2PbI_4$ and monolayer BP are both well maintained. Furthermore, it can be seen from the projected band structure that the electronic states of the BP layer (red line) dominate both the CBM and VBM of the $(PEA)_2PbI_4$/BP heterostructure, indicating a type-I band alignment with a significant offset on valence bands. From the DOS indicated in Figure 4, it was also found that both VBM and CBM of the $(PEA)_2PbI_4$/BP heterostructure are contributed by P elements consistent with the results of the projected band structure. In material and device design, semiconducting heterostructure band alignment and band offsets are even more essential than the band structures. Using the vacuum level as a common energy reference, we calculated the band alignment of the $(PEA)_2PbI_4$/BP heterostructure. As shown in Figure 5, our findings reveal that the CBM of BP is lower in energy than that of $(PEA)_2PbI_4$, while the VBM of BP is higher in energy than

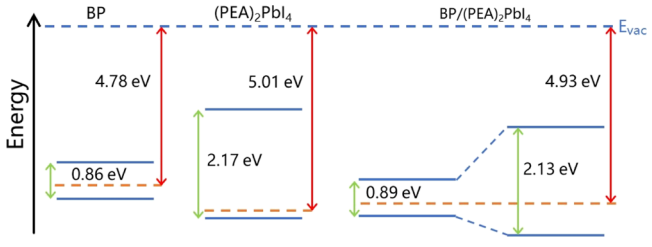

Figure 5. Band alignments of monolayer BP, monolayer $(PEA)_2PbI_4$, and the $(PEA)_2PbI_4$/BP heterostructure. Relevant electronic parameters are also given in the figure. The Fermi level is represented by red dashed lines. As a baseline, the vacuum level is used.

that of $(PEA)_2PbI_4$, which further demonstrates that the $(PEA)_2PbI_4$/BP heterostructure is a type-I heterostructure. According to Anderson limit,[65] the difference in electron affinity (in the *x*-direction) or ionization energy between the components of hetero 2D materials could be used to directly compute the conduction band offset and valence band offset of the heterostructure. The conduction (valence) band offset is defined as $\Delta E_C = E_{C\_B} - E_{C\_P}$ ($\Delta E_V = E_{V\_B} - E_{V\_P}$), where $E_{C\_P(B)}$ and $E_{V\_P(B)}$ are the CBM and VBM of $(PEA)_2PBI_4$(BP) in the $(PEA)_2PbI_4$/BP heterostructure. For the calculation of band offsets, the vacuum level is used as a common energy reference. The evaluated E_C and E_V of the $(PEA)_2PbI_4$/BP heterostructure in our example are 1.05 and 0.23 eV, respectively. Furthermore, the work function of the $(PEA)_2PbI_4$/BP heterostructure and its components is calculated according to the following equation

$$W = E_{vac} - E_F$$

where E_{vac} is the vacuum energy level and E_F is the Fermi level. Our results reveal that the work functions for the $(PEA)_2PbI_4$ monolayer and BP monolayer are 5.01 and 4.78 eV, respectively. The electrons move from the $(PEA)_2PbI_4$ layer to the BP layer, as indicated by the difference in work functions between $(PEA)_2PbI_4$ and BP. When the $(PEA)_2PbI_4$ monolayer and the BP monolayer come into contact, the Fermi level of $(PEA)_2PbI_4$ is pushed higher, while the Fermi level of BP is dragged down until the Fermi levels are balanced. In contact, the work function of the $(PEA)_2PbI_4$/BP heterostructure is 4.93 eV.

The 3D plot of differential charge density (DCD), which shows electron transport between the $(PEA)_2PbI_4$ and BP layers, was generated using the following formula

$$\Delta\rho = \rho_{hetero} - \rho_{perovskite} - \rho_{BP}$$

where ρ_{hetero}, $\rho_{perovskite}$, and ρ_{BP} are the electronic densities of the heterojunction, pure $(PEA)_2PbI_4$ monolayer, and BP monolayer, respectively. In the heterojunction, there is a redistribution of electron density between the $(PEA)_2PbI_4$ monolayer and the BP monolayer, as illustrated in Figure 6a. The plane-averaged density approaches zero when z is far enough away from the heterostructure interface. The 3D charge density difference is calculated in the same way as the plane-averaged charge density difference, which is displayed for comparison. As shown in Figure 6a, the charge is observed to increase toward the side of monolayer BP, whereas it is reduced near the side of monolayer $(PEA)_2PbI_4$, which means $(PEA)_2PbI_4$ forms a p-doping semiconductor after stacking with monolayer BP. Charge rearrangement, including charge depletion and buildup across the heterojunction, results in a built-in interfacial dipole. The plane-averaged electrostatic potential along the stacking direction is shown in Figure 6b. It clearly shows that there is a potential drop of 3.12 eV in the $(PEA)_2PbI_4$/BP heterostructure. The electrons may readily be driven from BP to $(PEA)_2PbI_4$ due to the potential drop. Given the synergistic impact on carrier transport, which is induced by the electrostatic potential drop, the transport performance could be improved in practical applications.

In electrical and optoelectronic devices, carrier mobility is also a significant factor. Herein, the Takagi model is used to determine carrier mobility based on Bardeen and Shockley's deformation potential theory.[64] The calculated carrier mobility of the heterostructure is summarized in Table 1. It finds that the electron mobility shows a remarkable anisotropy, with the

https://doi.org/10.1021/acsomega.1c02264
ACS Omega 2021, 6, 20877−20886

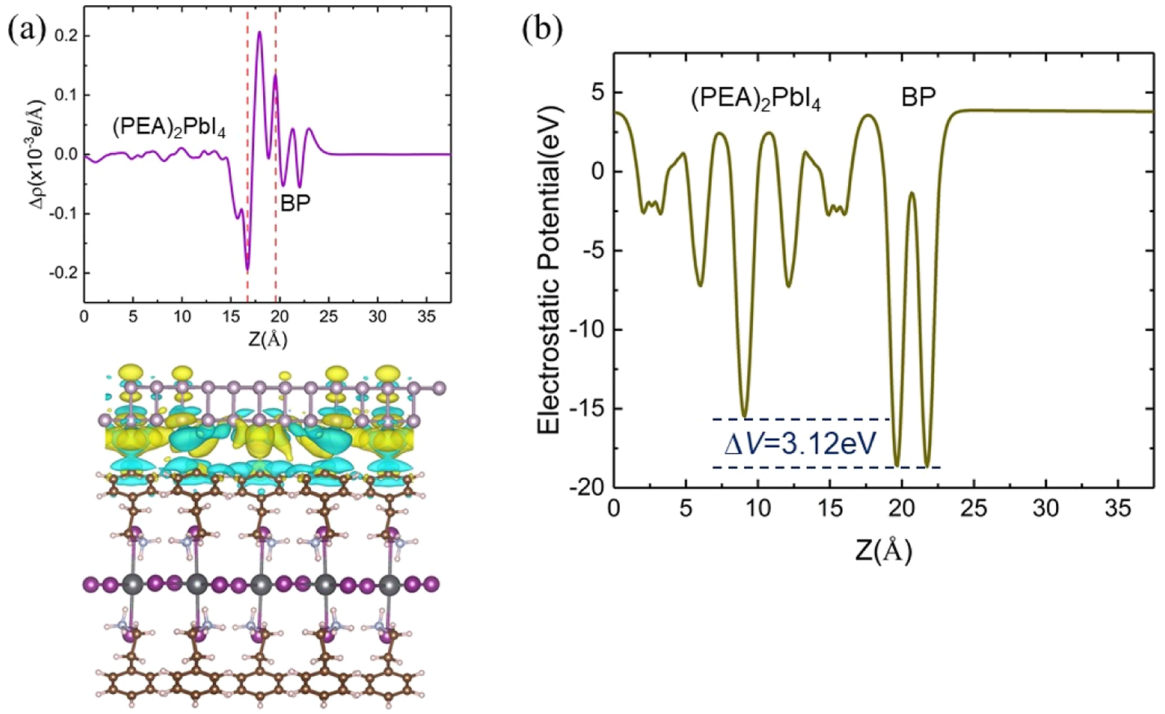

Figure 6. (a) Plane-averaged DCD of the $(PEA)_2PbI_4$/BP heterostructure as well as *z*-direction side views of the isosurfaces of DCD with an isosurface of 0.0001 e Å^{-3}. The gain of electrons is shown by the yellow zone, while the loss of electrons is indicated by the cyan region. (b) Electrostatic potential of the $(PEA)_2PbI_4$/BP heterostructure as a function of *z*-direction.

Table 1. Calculated Carrier Mobility of the $(PEA)_2PbI_4$/BP Heterostructure for the Electron (e) and Hole (h) along the *x*- and *y*-Direction[a]

carrier type	Direction	C_{2D} (J m^{-2})	m^* (m_0)	E_i (eV)	m_a (m_0)	μ_{2D} (10^3 cm^2 V^{-1} s^{-1})
e	*x*	269.65	1.247	5.186	0.486	0.356 (0.088)
	y	163.72	0.190	1.872	0.486	10.864 (1.123)
h	*x*	269.65	6.149	0.858	1.031	1.231 (15.518)
	y	163.72	0.173	4.892	1.031	1.345 (0.674)

[a]The cited carrier mobility of BP calculated by Qiao et al.[26] in brackets.

electron mobility in the *y*-direction being an order of magnitude larger than that in the *x*-direction. Moreover, the electron mobility of the heterostructure is extremely enhanced compared to that of free BP. The main reason for the large increase in electron mobility is that the total energy of the $(PEA)_2PbI_4$/BP heterostructure has remarkably changed when subjected to lattice deformation; hence, the value of the in-plane elastic modulus (in both *x*- and *y*-directions) also becomes very large. It also exhibits high hole mobility up to 10^3 cm^2 V^{-1} s^{-1} in both *x*- and *y*-directions. Compared with the monolayer BP, the hole carrier mobility for the heterojunction in the *y*-direction is larger, whereas the hole carrier mobility in the *x*-direction is smaller.

Because the exciton is one of the most crucial physical entities in the performance of optoelectronic and photonic devices, we calculated exciton binding energies (E_{eb}) of the $(PEA)_2PbI_4$ monolayer, BP monolayer, and $(PEA)_2PbI_4$/BP heterostructure based on the Wannier exciton model; the exciton binding energies are given as the formula[66]

$$E_{eb} = \frac{m_e e^4}{2(4\pi\varepsilon_0)^2\hbar^2}\frac{m_r^*}{m_e}\frac{1}{\varepsilon_\infty^{\,2}}\frac{1}{n^2} \approx 13.56\frac{m_r^*}{m_e}\frac{1}{\varepsilon_\infty^{\,2}}\frac{1}{n^2}$$

where m_r^* is the reduced exciton mass derived from the equation $\frac{1}{m_r^*} = \frac{1}{m_e^*} + \frac{1}{m_h^*}$ and ε_∞ is the static dielectric constant contributed from electrons, which can be evaluated by using density functional perturbation theory.[65,67−72] *n* is the exciton energy level. The calculated results are shown in Table 2. As the dimensionality of the system decreases, the Coulomb shielding effect will also weaken, resulting in a stronger exciton effect. For $(PEA)_2PbI_4$, the exciton energy 239 meV in this work agrees well with the exciton energy 272 meV calculated by Zhao et al.[62] In addition, for monolayer BP, the exciton binding energy is calculated to be 642 meV, which is comparable with other reported values.[73] As for the $(PEA)_2PbI_4$/BP heterostructures, it was found that the exciton

Table 2. Calculated Reduced Exciton Mass (m_r^*) Static Dielectric Constants in Direction *x* and *y*, (ε_∞^x and ε_∞^y), Average Static Dielectric Constants (ε_∞), and Exciton Binding Energies (E_{eb})

structure	m_r^* (m_0)	ε_∞^x	ε_∞^y	ε_∞	E_{eb} (meV)
$(PEA)_2PbI_4$	0.14	2.87	2.78	2.82	239
BP	0.58	2.73	4.28	3.50	642
$(PEA)_2PbI_4$/BP	0.58	4.18	4.83	4.51	386

https://doi.org/10.1021/acsomega.1c02264
ACS Omega 2021, 6, 20877−20886

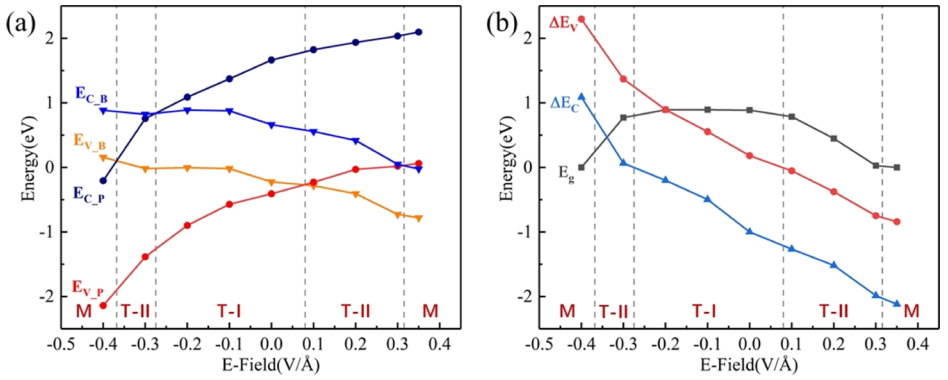

Figure 7. (a) Evolution of the band edges of BP and $(PEA)_2PbI_4$ in the $(PEA)_2PbI_4$/BP heterostructure as a function of the field. (b) Evolution of the band gap and band offsets of the $(PEA)_2PbI_4$/BP heterostructure as a function of the external field. $E_{C\_P(B)}$ and $E_{V\_P(B)}$ are the CBM and VBM of $(PEA)_2PbI_4$(BP) in the $(PEA)_2PbI_4$/BP heterostructure. The Fermi level is set as zero. The regions labeled M, T-I, and T-II are metal range, type-I band arrangement range, and type-II band arrangement range, respectively.

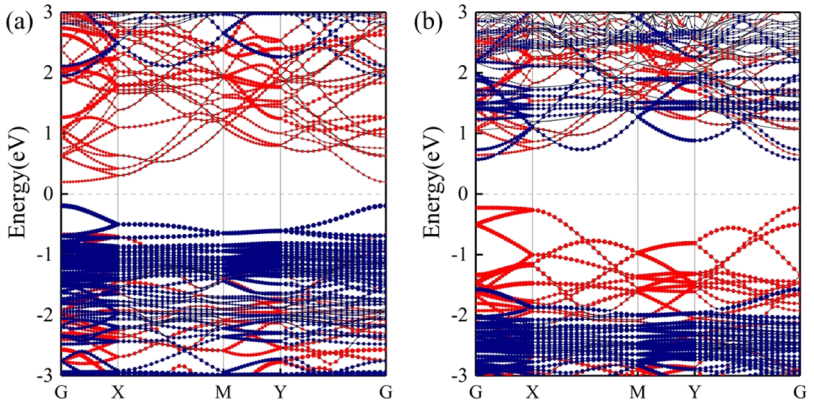

Figure 8. Calculated projected band structure under the electric field of (a) 0.2 and (b) −0.3 V/Å, respectively. The bands projected onto $(PEA)_2PbI_4$ and BP are rendered blue and red, respectively. The dot size reflects the weight of each species in the bands. The Fermi level (the dotted line) is set to zero.

binding energy is 386 meV, which is larger than that in 2D perovskite $(PEA)_2PbI_4$. Larger exciton binding energy may provide better application prospects in luminescence and laser.

Electric fields can be employed to control the electrical characteristics of vertical heterojunctions. We ran simulations in the $(PEA)_2PbI_4$/BP heterojunction with electric fields ranging from −0.4 to 0.35 V/Å in the vertical direction (z-direction). A positive electric field is applied with an interval step of 0.1 V/Å from the bottom $(PEA)_2PbI_4$ layer to the top BP layer, while the negative electric field is applied from the opposite direction. The plots in Figure 7 illustrate how an applied external perpendicular electric field ($E_\perp$) affects the electrical characteristics of the $(PEA)_2PbI_4$/BP heterostructure. The band edges of BP or $(PEA)_2PbI_4$ under various electric fields are calculated and shown in Figure 7a. First of all, the corresponding band gaps of $(PEA)_2PbI_4$ and BP are affected little by the external electric field. Second, the CBM and VBM of $(PEA)_2PbI_4$ both increase when the electric field increases, whereas the CBM and VBM of BP show a declining trend. Additionally, when $E_\perp$ is ∼−0.28 V/Å, the $(PEA)_2PbI_4$/BP heterojunction transitions from type-II to type-I, and when $E_\perp$ is ∼0.08 V/Å, it transitions from type-I to type-II, resulting in distinct spatial distributions of the lowest energy electrons and holes. When $E_\perp > 0.31$ V/Å or $E_\perp < -0.37$ V/Å, the band gap decreased to zero, which means the electronic property of the heterostructure is transferred from semiconductor to metal. To gain further insights, Figure 7b shows the evolution of the band gap (E_g) as a function of the external electric field. It has been discovered that when the electric fields increase, the band gap increases initially and then changes slowly. Our findings demonstrate that when the electric field is greater than 0.1 V/Å, the band gap decreases fast. Furthermore, ΔE_C and ΔE_V show similar variation trends and decrease linearly with $E_\perp$, as shown in Figure 7b. Due to the transition of the $(PEA)_2PbI_4$/BP heterostructure from metal to semiconductor under different vertical electric fields, field-effect transistors based on $(PEA)_2PbI_4$/BP with a super large current rectification effect can be designed, which reveals the great potential of logic device application. In addition, for medium electric fields from −0.3 to 0.15 V/Å, a large band gap of about 0.8−0.9 eV is found, which leads to obvious optical absorption characteristics of semiconductors, which is suitable for photovoltaic device application.

In order to give further support that the $(PEA)_2PbI_4$/BP heterostructure experiences a transition from type-I to type-II by applying the electric field, the band structures under the electric fields of 0.2 and −0.3 V/Å are shown in Figure 8a,b, respectively. Under an electric field of 0.2 V/Å, the CBM state of the $(PEA)_2PBI_4$/BP heterostructure is mostly contributed by BP, whereas the VBM state is mostly contributed by $(PEA)_2PBI_4$. In contrast, the CBM state was mainly provided by $(PEA)_2PBI_4$, while the VBM state was mostly provided by BP under an electric field of −0.3 V/Å. Therefore, the band type can be changed from type-I to type-II by an applied

https://doi.org/10.1021/acsomega.1c02264
ACS Omega 2021, 6, 20877−20886

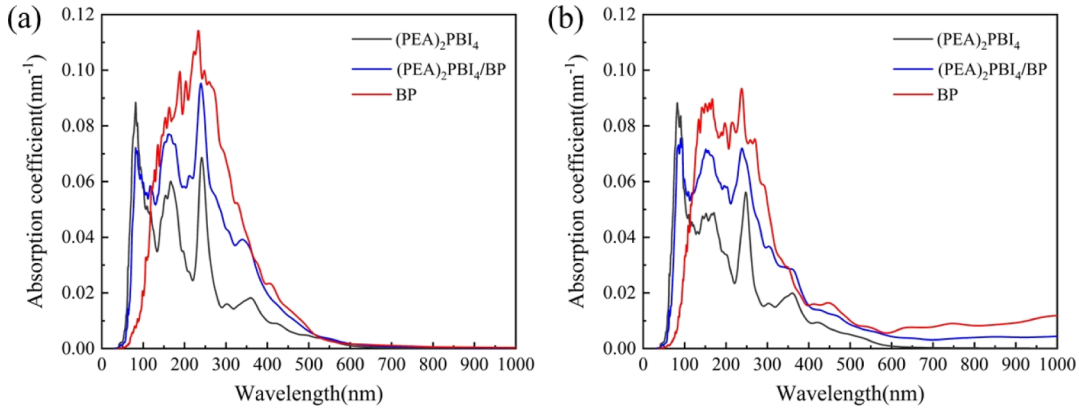

Figure 9. Absorption coefficient of monolayer BP, monolayer $(PEA)_2PbI_4$, and the $(PEA)_2PbI_4$/BP heterostructure in the (a) *x*-direction and (b) *y*-direction.

suitable electric field, which agrees with the results shown in Figure 7. Free electrons and holes will be spontaneously separated in the type-II heterostructure, preventing photogenerated electron and hole pairs from recombining. This is favorable to the separation and collection of electrons and holes in photovoltaic devices. The energy band structure of the $(PEA)_2PBI_4$/BP heterostructure can be effectively manipulated by the external electric field, which also provides more possibilities for the design of new optoelectronic devices.

The interlayer charge transfer and redistribution behaviors induced by the external electric field can be characterized by employing the plane-averaged DCD $\Delta\rho(z)$ along the *z*-direction perpendicular to the heterostructure surface. As depicted in Figure S4, it can be clearly seen that the charge transfer between the $(PEA)_2PBI_4$ and BP layer can be remarkably enhanced with the increase of the external electric field. By applying a positive electric field across the interface, electrons from the $(PEA)_2PbI_4$ layer are injected into the BP layer. Furthermore, when an electric field with the opposite direction is applied, the direction of charge transfer will shift.

3.3. Optical Properties. The optical absorption curves of monolayer BP, monolayer $(PEA)_2PbI_4$, and their heterostructure, as shown in Figure 9, are calculated to analyze the optical absorption properties of the 2D perovskite heterostructure and investigate the shift of the absorption spectrum. The absorption coefficient of monolayer BP is clearly larger than that of monolayer $(PEA)_2PbI_4$ perovskite materials, according to the results. The light absorptions of the heterostructure are due to the combination of monolayer $(PEA)_2PBI_4$ and BP, which exhibits a great potential application in solar cells. Therefore, combining BP and 2D perovskites to build heterostructures is an effective strategy for improving the light absorption of 2D perovskite devices, which shows a lot of potential in photovoltaic cells. Additionally, significant and anisotropic optical absorption is observed especially for monolayer BP and the heterostructure. For monolayer BP and the heterostructure, the absorption coefficient at the *x*-direction is larger than the absorption coefficient at the *y*-direction in the wavelength range 0−450 nm, while the absorption curves at the *y*-direction show a larger absorption coefficient in the wavelength range >450 nm and a longer absorption edge wavelength than the absorption curves at the *x*-direction.

4. CONCLUSIONS

In summary, using first-principles calculations, the equilibrium structure, electrical characteristics, and optical properties of the $(PEA)_2PbI_4$/BP heterostructure are explored. According to our results, the $(PEA)_2PbI_4$/BP heterostructure is very stable at room temperature. The type-I band arrangement and excellent carrier mobility of the $(PEA)_2PbI_4$/BP heterostructure are both present. Our results also demonstrated that the synergistic impact on carrier transport caused by the electrostatic potential drop in the PN junction produced between these two layers could improve transport performance in practical applications. More importantly, an external electric field can effectively modulate the band offset and band gap of the heterostructure, with the transition from semiconductor to metal. The changes in band edges of $(PEA)_2PbI_4$ and BP in $(PEA)_2PbI_4$/BP, which appear to vary with the external electric field, provide further insights. As for $(PEA)_2PbI_4$/BP heterostructures, the larger exciton binding energy may have better application prospects in luminescence and laser. Besides, we also found that we can effectively enhance the intensity of the light absorptions by building a $(PEA)_2PBI_4$/BP heterostructure compared to the pure 2D perovskite. Our theoretical results may inspire much interest in experimental research of the $(PEA)_2PBI_4$/BP vdW heterostructure and will present abundant opportunities for the application in future optoelectronics such as a photodetector, photovoltaic cell, and luminescent device.

■ ASSOCIATED CONTENT

Supporting Information

The Supporting Information is available free of charge at https://pubs.acs.org/doi/10.1021/acsomega.1c02264.

Calculated lattice parameters (*a*, *b*) of monolayer $(PEA)_2PbI_4$, BP monolayer, and $(PEA)_2PbI_4$/BP heterostructure; calculated energy band structures of monolayer $(PEA)_2PbI_4$ and monolayer BP; band edge energy shift of VBM and CBM; total energy of the $(PEA)_2PBI_4$/BP heterostructure; and plane-averaged differential charge density (PDF)

https://doi.org/10.1021/acsomega.1c02264
ACS Omega 2021, 6, 20877−20886

AUTHOR INFORMATION

Corresponding Authors

Dan Li − *Department of Physics, Beijing Jiaotong University, Beijing 100044, China;* orcid.org/0000-0001-7661-0364; Email: danli@bjtu.edu.cn

Chunjun Liang − *Key Laboratory of Luminescence and Optical Information, Ministry of Education, Beijing Jiaotong University, Beijing 100044, China;* orcid.org/0000-0003-4557-0106; Email: chjliang@bjtu.edu.cn

Authors

Dong Li − *Department of Physics, Beijing Jiaotong University, Beijing 100044, China*

Anqi Yang − *Department of Physics, Beijing Jiaotong University, Beijing 100044, China*

He Zhang − *Department of Physics, Beijing Jiaotong University, Beijing 100044, China*

Xinxin Lai − *Department of Physics, Beijing Jiaotong University, Beijing 100044, China*

Complete contact information is available at: https://pubs.acs.org/10.1021/acsomega.1c02264

Notes

The authors declare no competing financial interest.

The data that support the findings of this study are available from the corresponding author upon reasonable request.

ACKNOWLEDGMENTS

The authors acknowledge the financial support from the National Natural Science Foundation of China (nos. 61874008 and 61574014) and the Beijing Municipal Science and Technology Commission project (no. Z181100004718004).

REFERENCES

(1) Liao, H.-C.; Tam, T. L. D.; Guo, P.; Wu, Y.; Manley, E. F.; Huang, W.; Zhou, N.; Soe, C. M. M.; Wang, B.; Wasielewski, M. R.; et al. Dopant-Free Hole Transporting Polymers for High Efficiency, Environmentally Stable Perovskite Solar Cells. *Adv. Energy Mater.* **2016**, *6*, 1600502.

(2) Tsai, H.; Asadpour, R.; Blancon, J.-C.; Stoumpos, C. C.; Durand, O.; Strzalka, J. W.; Chen, B.; Verduzco, R.; Ajayan, P. M.; Tretiak, S.; et al. Light-induced lattice expansion leads to high-efficiency perovskite solar cells. *Science* **2018**, *360*, 67.

(3) Kojima, A.; Teshima, K.; Shirai, Y.; Miyasaka, T. Organometal Halide Perovskites as Visible-Light Sensitizers for Photovoltaic Cells. *J. Am. Chem. Soc.* **2009**, *131*, 6050−6051.

(4) Yang, D.; Yang, R.; Wang, K.; Wu, C.; Zhu, X.; Feng, J.; Ren, X.; Fang, G.; Priya, S.; Liu, S. High efficiency planar-type perovskite solar cells with negligible hysteresis using EDTA-complexed SnO2. *Nat. Commun.* **2018**, *9*, 3239.

(5) Xing, G.; Mathews, N.; Sun, S.; Lim, S. S.; Lam, Y. M.; Grätzel, M.; Mhaisalkar, S.; Sum, T. C. Long-Range Balanced Electron- and Hole-Transport Lengths in Organic-Inorganic $CH_3NH_3PbI_3$. *Science* **2013**, *342*, 344.

(6) Green, M.; Dunlop, E.; Hohl-Ebinger, J.; Yoshita, M.; Kopidakis, N.; Hao, X. Solar cell efficiency tables (Version 55). *Prog. Photovoltaics* **2020**, *29*, 3−15.

(7) Chen, Y.; Sun, Y.; Peng, J.; Tang, J.; Zheng, K.; Liang, Z. 2D Ruddlesden−Popper Perovskites for Optoelectronics. *Adv. Mater.* **2018**, *30*, 1703487.

(8) Straus, D. B.; Kagan, C. R. Electrons, Excitons, and Phonons in Two-Dimensional Hybrid Perovskites: Connecting Structural, Optical, and Electronic Properties. *J. Phys. Chem. Lett.* **2018**, *9*, 1434−1447.

(9) Saparov, B.; Mitzi, D. B. Organic−Inorganic Perovskites: Structural Versatility for Functional Materials Design. *Chem. Rev.* **2016**, *116*, 4558−4596.

(10) Straus, D. B.; Iotov, N.; Gau, M. R.; Zhao, Q.; Carroll, P. J.; Kagan, C. R. Longer Cations Increase Energetic Disorder in Excitonic 2D Hybrid Perovskites. *J. Phys. Chem. Lett.* **2019**, *10*, 1198−1205.

(11) Peng, W.; Yin, J.; Ho, K.-T.; Ouellette, O.; De Bastiani, M.; Murali, B.; El Tall, O.; Shen, C.; Miao, X.; Pan, J.; et al. Ultralow Self-Doping in Two-dimensional Hybrid Perovskite Single Crystals. *Nano Lett.* **2017**, *17*, 4759−4767.

(12) Cheng, B.; Li, T.-Y.; Wei, P.-C.; Yin, J.; Ho, K.-T.; Retamal, J. R. D.; Mohammed, O. F.; He, J.-H. Layer-edge device of two-dimensional hybrid perovskites. *Nat. Commun.* **2018**, *9*, 5196.

(13) Niu, W.; Eiden, A.; Vijaya Prakash, G.; Baumberg, J. J. Exfoliation of self-assembled 2D organic-inorganic perovskite semiconductors. *Appl. Phys. Lett.* **2014**, *104*, 171111.

(14) Dou, L.; Wong, A. B.; Yu, Y.; Lai, M.; Kornienko, N.; Eaton, S. W.; Fu, A.; Bischak, C. G.; Ma, J.; Ding, T.; et al. Atomically thin two-dimensional organic-inorganic hybrid perovskites. *Science* **2015**, *349*, 1518.

(15) Liu, B.; Long, M.; Cai, M.-Q.; Yang, J. Two-Dimensional van der Waals Heterostructures Constructed via Perovskite $(C_4H_9NH_3)_2XBr_4$ and Black Phosphorus. *J. Phys. Chem. Lett.* **2018**, *9*, 4822−4827.

(16) Tsai, H.; Nie, W.; Blancon, J.-C.; Stoumpos, C. C.; Asadpour, R.; Harutyunyan, B.; Neukirch, A. J.; Verduzco, R.; Crochet, J. J.; Tretiak, S.; Pedesseau, L.; Even, J.; et al. High-efficiency two-dimensional Ruddlesden−Popper perovskite solar cells. *Nature* **2016**, *536*, 312−316.

(17) Stoumpos, C. C.; Cao, D. H.; Clark, D. J.; Young, J.; Rondinelli, J. M.; Jang, J. I.; Hupp, J. T.; Kanatzidis, M. G. Ruddlesden−Popper Hybrid Lead Iodide Perovskite 2D Homologous Semiconductors. *Chem. Mater.* **2016**, *28*, 2852−2867.

(18) Sanehira, Y.; Numata, Y.; Ikegami, M.; Miyasaka, T. Photovoltaic Properties of Two-dimensional $(CH_3(CH_2)_3NH_3)_2PbI_4$ Perovskite Crystals Oriented with TiO_2 Nanowire Array. *Chem. Lett.* **2017**, *46*, 1204−1206.

(19) Coleman, J. N.; Lotya, M.; O'Neill, A.; Bergin, S. D.; King, P. J.; Khan, U.; Young, K.; Gaucher, A.; De, S.; Smith, R. J.; Shvets, I. V.; et al. Two-Dimensional Nanosheets Produced by Liquid Exfoliation of Layered Materials. *Science* **2011**, *331*, 568.

(20) Liu, H.; Neal, A. T.; Zhu, Z.; Luo, Z.; Xu, X.; Tománek, D.; Ye, P. D. Phosphorene: An Unexplored 2D Semiconductor with a High Hole Mobility. *ACS Nano* **2014**, *8*, 4033−4041.

(21) Mak, K. F.; Lee, C.; Hone, J.; Shan, J.; Heinz, T. F. Atomically Thin MoS_2: A New Direct-Gap Semiconductor. *Phys. Rev. Lett.* **2010**, *105*, 136805.

(22) Tsai, D.-S.; Liu, K.-K.; Lien, D.-H.; Tsai, M.-L.; Kang, C.-F.; Lin, C.-A.; Li, L.-J.; He, J.-H. Few-Layer MoS_2 with High Broadband Photogain and Fast Optical Switching for Use in Harsh Environments. *ACS Nano* **2013**, *7*, 3905−3911.

(23) Wang, Q. H.; Kalantar-Zadeh, K.; Kis, A.; Coleman, J. N.; Strano, M. S. Electronics and optoelectronics of two-dimensional transition metal dichalcogenides. *Nat. Nanotechnol.* **2012**, *7*, 699−712.

(24) Castellanos-Gomez, A.; Vicarelli, L.; Prada, E.; Island, J. O.; Narasimha-Acharya, K. L.; Blanter, S. I.; Groenendijk, D. J.; Buscema, M.; Steele, G. A.; Alvarez, J. V.; et al. Isolation and characterization of few-layer black phosphorus. *2D Mater.* **2014**, *1*, 025001.

(25) Li, L.; Yu, Y.; Ye, G. J.; Ge, Q.; Ou, X.; Wu, H.; Feng, D.; Chen, X. H.; Zhang, Y. Black phosphorus field-effect transistors. *Nat. Nanotechnol.* **2014**, *9*, 372−377.

(26) Qiao, J.; Kong, X.; Hu, Z.-X.; Yang, F.; Ji, W. High-mobility transport anisotropy and linear dichroism in few-layer black phosphorus. *Nat. Commun.* **2014**, *5*, 4475.

(27) Buscema, M.; Groenendijk, D. J.; Blanter, S. I.; Steele, G. A.; van der Zant, H. S. J.; Castellanos-Gomez, A. Fast and Broadband Photoresponse of Few-Layer Black Phosphorus Field-Effect Transistors. *Nano Lett.* **2014**, *14*, 3347−3352.

(28) Behera, S. K.; Deb, P. Controlling the bandgap in graphene/h-BN heterostructures to realize electron mobility for high performing FETs. *RSC Adv.* **2017**, *7*, 31393−31400.
(29) Chen, X.; Wu, Y.; Wu, Z.; Han, Y.; Xu, S.; Wang, L.; Ye, W.; Han, T.; He, Y.; Cai, Y.; Wang, N. High-quality sandwiched black phosphorus heterostructure and its quantum oscillations. *Nat. Commun.* **2015**, *6*, 7315.
(30) You, B.; Wang, X.; Zheng, Z.; Mi, W. Black phosphorene/monolayer transition-metal dichalcogenides as two dimensional van der Waals heterostructures: a first-principles study. *Phys. Chem. Chem. Phys.* **2016**, *18*, 7381−7388.
(31) Tang, K.; Qi, W.; Li, Y.; Wang, T. Electronic Properties of van der Waals Heterostructure of Black Phosphorus and MoS_2. *J. Phys. Chem. C* **2018**, *122*, 7027−7032.
(32) Huang, L.; Huo, N.; Li, Y.; Chen, H.; Yang, J.; Wei, Z.; Li, J.; Li, S.-S. Electric-Field Tunable Band Offsets in Black Phosphorus and MoS_2 van der Waals p-n Heterostructure. *J. Phys. Chem. Lett.* **2015**, *6*, 2483−2488.
(33) Fang, C.; Wang, H.; Shen, Z.; Shen, H.; Wang, S.; Ma, J.; Wang, J.; Luo, H.; Li, D. High-Performance Photodetectors Based on Lead-Free 2D Ruddlesden−Popper Perovskite/MoS_2 Heterostructures. *ACS Appl. Mater. Interfaces* **2019**, *11*, 8419−8427.
(34) Chen, Y.; Ma, J.; Liu, Z.; Li, J.; Duan, X.; Li, D. Manipulation of Valley Pseudospin by Selective Spin Injection in Chiral Two-Dimensional Perovskite/Monolayer Transition Metal Dichalcogenide Heterostructures. *ACS Nano* **2020**, *14*, 15154−15160.
(35) Chen, Y.; Liu, Z.; Li, J.; Cheng, X.; Ma, J.; Wang, H.; Li, D. Robust Interlayer Coupling in Two-Dimensional Perovskite/Monolayer Transition Metal Dichalcogenide Heterostructures. *ACS Nano* **2020**, *14*, 10258−10264.
(36) Zhang, Q.; Linardy, E.; Wang, X.; Eda, G. Excitonic Energy Transfer in Heterostructures of Quasi-2D Perovskite and Monolayer WS_2. *ACS Nano* **2020**, *14*, 11482−11489.
(37) Min, L.; E, X. Y.; Xi, S. Y. Tunable band gap of MoS_2-SiC van der Waals heterostructures under normal strain and an external electric field. *AIP Adv.* **2017**, *7*, 015116.
(38) Geim, A. K.; Grigorieva, I. V. Van der Waals heterostructures. *Nature* **2013**, *499*, 419−425.
(39) Peng, Q.; Wang, Z.; Sa, B.; Wu, B.; Sun, Z. Electronic structures and enhanced optical properties of blue phosphorene/transition metal dichalcogenides van der Waals heterostructures. *Sci. Rep.* **2016**, *6*, 31994.
(40) Novoselov, K. S.; Mishchenko, A.; Carvalho, A.; Castro Neto, A. H. 2D materials and van der Waals heterostructures. *Science* **2016**, *353*, aac9439.
(41) Chiu, M.-H.; Li, M.-Y.; Zhang, W.; Hsu, W.-T.; Chang, W.-H.; Terrones, M.; Terrones, H.; Li, L.-J. Spectroscopic Signatures for Interlayer Coupling in MoS_2−WSe_2 van der Waals Stacking. *ACS Nano* **2014**, *8*, 9649−9656.
(42) Jin, C.; Kim, J.; Suh, J.; Shi, Z.; Chen, B.; Fan, X.; Kam, M.; Watanabe, K.; Taniguchi, T.; Tongay, S.; Zettl, A.; Wu, J.; Wang, F. Interlayer electron−phonon coupling in WSe_2/hBN heterostructures. *Nat. Phys.* **2017**, *13*, 127−131.
(43) Liu, Y.; Su, H.; Ma, C.; Ji, D.; Zheng, X.; Wang, P.; Zheng, S.; Wang, L.; Wang, Z.; Xu, D. IQGAP1 mediates podocyte injury in diabetic kidney disease by regulating nephrin endocytosis. *Cell. Signalling* **2019**, *59*, 13−23.
(44) Seo, S.; Kim, S.; Choi, H.; Lee, J.; Yoon, H.; Piao, G.; Park, J. C.; Jung, Y.; Song, J.; Jeong, S. Y.; Park, H.; Lee, S. Direct In Situ Growth of Centimeter-Scale Multi-Heterojunction MoS2/WS2/WSe2 Thin-Film Catalyst for Photo-Electrochemical Hydrogen Evolution. *Adv. Sci.* **2019**, *6*, 1900301.
(45) Georgiou, T.; Jalil, R.; Belle, B. D.; Britnell, L.; Gorbachev, R. V.; Morozov, S. V.; Kim, Y.-J.; Gholinia, A.; Haigh, S. J.; Makarovsky, O.; Eaves, L.; Ponomarenko, L. A.; Geim, A. K.; Novoselov, K. S.; Mishchenko, A. Vertical field-effect transistor based on graphene−WS_2 heterostructures for flexible and transparent electronics. *Nat. Nanotechnol.* **2013**, *8*, 100−103.
(46) Padilha, J. E.; Fazzio, A.; da Silva, A. J. R. van der Waals Heterostructure of Phosphorene and Graphene: Tuning the Schottky Barrier and Doping by Electrostatic Gating. *Phys. Rev. Lett.* **2015**, *114*, 066803.
(47) Sinha, S.; Arora, S. K.; Wu, H.-C.; Sathe, V. G. Phonon scattering mechanism in van der Waals heterostructures comprising of MoS_2 and WS_2 nanosheets. *Mater. Today: Proc.* **2021**, *45*, 4612−4618.
(48) Liu, H.; Gao, R.; Yang, J.; Yang, F.; Wang, T.; Zhang, Z.; Liu, X.; Jia, H.; Xu, B.; Ma, H. Graphene/α-tellurene van der Waals heterobilayers: Interlayer coupling and gate-tunable carrier type and Schottky barriers. *Appl. Surf. Sci.* **2020**, *525*, 146476.
(49) Liu, X.-Y.; Zeng, H.-D.; Zhang, H.; Cheng, X.-L. Tunable electronic properties of two-dimensional type-I 1T-SN_2/hBN and type-II 1T-XN_2/hBN (X = Se, Te) van der Waals heterostructures from first-principle study. *Appl. Surf. Sci.* **2021**, *542*, 148659.
(50) Lv, Q.; Yan, F.; Mori, N.; Zhu, W.; Hu, C.; Kudrynskyi, Z. R.; Kovalyuk, Z. D.; Patanè, A.; Wang, K. Interlayer Band-to-Band Tunneling and Negative Differential Resistance in van der Waals BP/InSe Field-Effect Transistors. *Adv. Funct. Mater.* **2020**, *30*, 1910713.
(51) Yuan, J.; Najmaei, S.; Zhang, Z.; Zhang, J.; Lei, S.; Ajayan, P. M.; Yakobson, B. I.; Lou, J. Photoluminescence Quenching and Charge Transfer in Artificial Heterostacks of Monolayer Transition Metal Dichalcogenides and Few-Layer Black Phosphorus. *ACS Nano* **2015**, *9*, 555−563.
(52) Kresse, G.; Furthmüller, J. Efficiency of ab-initio total energy calculations for metals and semiconductors using a plane-wave basis set. *Comput. Mater. Sci.* **1996**, *6*, 15−50.
(53) Blöchl, P. E. Projector augmented-wave method. *Phys. Rev. B: Condens. Matter Mater. Phys.* **1994**, *50*, 17953−17979.
(54) Perdew, J. P.; Burke, K.; Ernzerhof, M. Generalized Gradient Approximation Made Simple. *Phys. Rev. Lett.* **1996**, *77*, 3865−3868.
(55) Grimme, S.; Antony, J.; Ehrlich, S.; Krieg, H. A consistent and accurate ab initio parametrization of density functional dispersion correction (DFT-D) for the 94 elements H-Pu. *J. Chem. Phys.* **2010**, *132*, 154104.
(56) Lee, M. M.; Teuscher, J.; Miyasaka, T.; Murakami, T. N.; Snaith, H. J. Efficient Hybrid Solar Cells Based on Meso-Superstructured Organometal Halide Perovskites. *Science* **2012**, *338*, 643.
(57) Mosconi, E.; Amat, A.; Nazeeruddin, M. K.; Grätzel, M.; De Angelis, F. First-Principles Modeling of Mixed Halide Organometal Perovskites for Photovoltaic Applications. *J. Phys. Chem. C* **2013**, *117*, 13902−13913.
(58) Schulz, P.; Edri, E.; Kirmayer, S.; Hodes, G.; Cahen, D.; Kahn, A. Interface energetics in organo-metal halide perovskite-based photovoltaic cells. *Energy Environ. Sci.* **2014**, *7*, 1377−1381.
(59) Even, J.; Pedesseau, L.; Jancu, J.-M.; Katan, C. Importance of Spin−Orbit Coupling in Hybrid Organic/Inorganic Perovskites for Photovoltaic Applications. *J. Phys. Chem. Lett.* **2013**, *4*, 2999−3005.
(60) Martyna, G. J.; Klein, M. L.; Tuckerman, M. Nosé−Hoover chains: The canonical ensemble via continuous dynamics. *J. Chem. Phys.* **1992**, *97*, 2635−2643.
(61) Yin, J.; Maity, P.; Naphade, R.; Cheng, B.; He, J.-H.; Bakr, O. M.; Brédas, J.-L.; Mohammed, O. F. Tuning Hot Carrier Cooling Dynamics by Dielectric Confinement in Two-Dimensional Hybrid Perovskite Crystals. *ACS Nano* **2019**, *13*, 12621−12629.
(62) Zhao, Y.-Q.; Ma, Q.-R.; Liu, B.; Yu, Z.-L.; Yang, J.; Cai, M.-Q. Layer-dependent transport and optoelectronic property in two-dimensional perovskite: $(PEA)_2PbI_4$. *Nanoscale* **2018**, *10*, 8677−8688.
(63) Bruzzone, S.; Fiori, G. Ab-initio simulations of deformation potentials and electron mobility in chemically modified graphene and two-dimensional hexagonal boron-nitride. *Appl. Phys. Lett.* **2011**, *99*, 222108.
(64) Bardeen, J.; Shockley, W. Deformation Potentials and Mobilities in Non-Polar Crystals. *Phys. Rev.* **1950**, *80*, 72−80.
(65) Zhou, W.-X.; Chen, K.-Q.; Tang, L.-M.; Yao, L.-J. Phonon thermal transport in InAs nanowires with different size and growth directions. *Phys. Lett. A* **2013**, *377*, 3144−3147.
(66) Jong, U.-G.; Yu, C.-J.; Ri, J.-S.; Kim, N.-H.; Ri, G.-C. Influence of halide composition on the structural, electronic, and optical

https://doi.org/10.1021/acsomega.1c02264
ACS Omega 2021, 6, 20877−20886

properties of mixed $CH_3NH_3Pb(I_{1-x}Br_x)_3$perovskites calculated using the virtual crystal approximation method. *Phys. Rev. B* **2016**, *94*, 125139.
(67) Zhao, Y.-Q.; Wang, X.; Liu, B.; Yu, Z.-L.; He, P.-B.; Wan, Q.; Cai, M.-Q.; Yu, H.-L. Geometric structure and photovoltaic properties of mixed halide germanium perovskites from theoretical view. *Org. Electron.* **2018**, *53*, 50−56.
(68) Cai, M.-Q.; Du, Y.; Huang, B.-Y. First-principles study of the critical thickness in asymmetric ferroelectric tunnel junctions. *Appl. Phys. Lett.* **2011**, *98*, 102907.
(69) Cao, D.; Cai, M.-Q.; Hu, W.-Y.; Peng, J.; Zheng, Y.; Huang, H.-T. Uniaxial strain-modulated conductivity in manganite superlattice ($LaMnO_3/SrMnO_3$). *Appl. Phys. Lett.* **2011**, *98*, 031910.
(70) Ying, H.; Zhou, W.-X.; Chen, K.-Q.; Zhou, G. Negative differential resistance induced by the Jahn−Teller effect in single molecular coulomb blockade devices. *Comput. Mater. Sci.* **2014**, *82*, 33−36.
(71) Zhao, Y.-Q.; Liu, B.; Yu, Z.-L.; Ma, J.; Wan, Q.; He, P.-b.; Cai, M.-Q. Strong ferroelectric polarization of $CH_3NH_3GeI_3$ with high-absorption and mobility transport anisotropy: theoretical study. *J. Mater. Chem. C* **2017**, *5*, 5356−5364.
(72) Baroni, S.; Resta, R. Ab initio calculation of the macroscopic dielectric constant in silicon. *Phys. Rev. B: Condens. Matter Mater. Phys.* **1986**, *33*, 7017−7021.
(73) Choi, J.-H.; Cui, P.; Lan, H.; Zhang, Z. Linear Scaling of the Exciton Binding Energy versus the Band Gap of Two-Dimensional Materials. *Phys. Rev. Lett.* **2015**, *115*, 066403.

https://doi.org/10.1021/acsomega.1c02264
ACS Omega 2021, 6, 20877−20886